International Journal of Solids and Structures 84 (2016) 147–159

Contents lists available at ScienceDirect

International Journal of Solids and Structures

journal homepage: www.elsevier.com/locate/ijsolstr

Mixed-mode traction-separation relations between graphene and copper by blister tests

Zhiyi Cao[a], Li Tao[b], Deji Akinwande[b], Rui Huang[a], Kenneth M. Liechti[a,*]

[a] Department of Aerospace Engineering and Engineering Mechanics, Research Center for the Mechanics of Solids, Structures and Materials, The University of Texas at Austin, Austin, Texas 78712, United States

[b] Department of Electrical and Computer Engineering, The University of Texas at Austin, Austin, Texas 78712, United States

ARTICLE INFO

Article history:
Received 5 September 2015
Revised 26 January 2016
Available online 4 February 2016

Keywords:
Graphene adhesion
Blister test
Fracture mode-mix
Cohesive zone modeling

ABSTRACT

A blister test with associated analysis was developed to characterize the traction-separation relations associated with interactions between graphene and a copper substrate to which it had been transferred. Graphene grown by chemical vapor deposition was backed by a photoresist film and transferred to a highly polished copper substrate from its seed copper foil. The graphene/photoresist composite film was then pressurized with deionized water through a hole in the substrate. The blister profiles and normal crack opening displacements (NCOD) were measured by two microscopes with synchronized cameras. Different mixed-mode conditions were achieved by varying the thickness of the backing layers. The measured adhesion energy for the graphene/copper and photoresist/copper interfaces showed a strong dependence on the mode-mix. Cohesive zone models associated with traction-separation relations were then developed to study the damage initiation and crack propagation under various mixed-mode conditions. The numerical solutions for the resistance curves, pressure *vs.* deflection, and NCOD were in good agreement with measurements. The cohesive zone model was extended to a wider range of mode-mixes by making use of the asperity locking model which had provided a mechanism for the observed toughening effect. The interactions between graphene and copper were found to be stronger in all respects than those associated with photoresist and copper. Because the monolayer graphene was sandwiched between photoresist and copper, this result suggests that graphene was not transparent to interactions between photoresist and copper, but opaque. The use of pressure could provide another approach to transfer large-scale graphene.

1. Introduction

Graphene is a single layer of carbon atoms arranged in a regular hexagonal pattern. It was first isolated and observed (Novoselov et al., 2004) by using scotch tape to mechanically exfoliate graphite multiple times until the number of graphene layers was reduced to one or a few layers. Substantial research since then has shown that graphene has exceptional electronic, mechanical, and thermal properties (Allen et al., 2009; Geim and Novoselov, 2007; Novoselov et al., 2012; Randviir et al., 2014).

For scaled applications, graphene will be grown on one seed substrate and then transferred to a target substrate; this motivates determining the interactions between graphene and various substrate materials in order to design for or otherwise facilitate successful transfer. Due to its high flexibility, graphene can conform more closely to a surface than conventional materials (Lui et al., 2009). This provides an opportunity to study short-range interactions like van der Waals or Casimir forces. Experimental work on graphene adhesion was initially focused on the measurement of adhesion energies between graphene and various substrates. By intercalating nanoparticles between graphene and silicon, Zong et al. (2010) reported the adhesion energy to be 0.151 J/m^2. Koenig et al. (2011) measured the adhesion energy of micromechanically exfoliated graphene on SiO_2, finding 0.45 J/m^2 for monolayer graphene and 0.31 J/m^2 for two to five layer graphene. Li et al. (2013) transferred CVD graphene onto a silicon wafer with an array of gold nano-pillars and an adhesion energy of 0.45 J/m^2 was extracted by measuring the diameter of the blisters. Cao et al. (2014) measured the adhesion of large-scale transferred graphene on a copper substrate, and obtained an adhesion energy of 0.341 J/m^2. Na et al. studied the interaction of wet-transferred graphene on silicon (Na et al., 2014), where an adhesion energy of 0.357 J/m^2 is in the range of van der Waals forces; however, the low strength (~5 MPa) and the long interaction ranges (~0.5 μm) of the associated traction-separation relations that were determined suggest

* Corresponding author. Tel.: +15124714164.
E-mail address: kml@mail.utexas.edu (K.M. Liechti).

http://dx.doi.org/10.1016/j.ijsolstr.2016.01.023
0020-7683/

other mechanisms. The various adhesion energies obtained could be due to contamination, surface roughness, or liquid trapped between graphene and the substrate. As will be borne out in this study, they may also reflect a dependence on the fracture mode-mix.

Theoretical analyses of interactions between graphene and substrates have been mainly focused on the mechanism of adhesion, the effect of substrate roughness and the number of graphene layers. Density function theory (DFT) has been widely used for studying interfacial adhesion. The adhesion between graphene and silicon oxide was investigated (Gao et al., 2014) by DFT with dispersion correction, which concluded that the van der Waals interaction is the predominant mechanism. Rudenko et al. (2011) studied the morphology effect on graphene/mica interactions. The effect of water between the interfaces was also investigated. Because most of the experiments on graphene adhesion were conducted in ambient environments, it is highly possible that water condensed between the interfaces. Water cavitation and bridging during the interfacial debonding could lead to lower strength and longer range of interactions (Cicero et al., 2008; Gao et al., 2015; Leenaerts et al., 2009; Wehling et al., 2008). A continuum mechanics approach was used to explain (Gao and Huang, 2011) the dependence of adhesion energy on the number of graphene layers observed in (Koenig et al., 2011). They considered the interactions between graphene and a corrugated surface, and concluded that multilayer graphene conforms less to the substrate, thereby lowering the adhesion energy.

In order to detach graphene from a substrate, a crack propagates along the graphene/substrate interface, so interfacial fracture mechanics applies. The mismatch of the material mechanical properties and the fact that the crack is constrained to grow along the interface result in a relatively complicated stress state at the crack tip. Interfacial fracture is often governed by a combination of local mode I (tension) and modes II and III (forward and out-of-plane shear) effects. The two main methodologies applied to study interfacial fracture are linear elastic fracture mechanics (LEFM) and cohesive zone modeling.

The LEFM approach to solving problems like cracks between two dissimilar materials was first adopted by Williams (1959) who established the oscillatory stress state near the crack tip by using a biharmonic stress function. Erdogan (1965) used the complex variable method and examined the stress distribution in two dissimilar half planes with a finite number of straight-line segments. Dundurs established the two parameters that characterize the elastic mismatch of a bimaterial pair (Dundurs and Bogy, 1969). A general description of the stresses and displacements near interfacial crack tips was developed based on LEFM concepts (Rice, 1988). Hutchinson and Suo reviewed developments in interfacial fracture mechanics and presented (Hutchinson and Suo, 1992) a series of formulas for the energy release rate and stress intensity factors for a number of interfacial crack configurations and sandwich specimens. Mixed-mode stress intensity factors are used to characterize stress state near the crack tip. Mixed-mode conditions are defined by a phase angle depending on the ratio between the shear and tensile stress intensity factors with a characteristic length scale for the crack. For a crack in a homogenous body, mixed-mode conditions are introduced by multiaxial remote loading conditions (Suresh et al., 1990). However, the material mismatch associated with interfacial cracks leads to mixed-mode conditions, even under global tension or shear.

Although the LEFM approach can provide the analytical stress state near the crack tip and energy release rate, it can only predict the onset of crack growth from a preexisting flaw. However the development of damage zones due to microbridging or plasticity ahead of the crack tip leads to a more gradual development of crack growth (Zhu et al., 2009). Cohesive zone modeling accounts for the development of inelastic effects and can therefore predict the gradual transition to steady state or fast fracture. The stress singularity at the tips of cracks in elastic bodies were first eliminated (Barenblatt, 1959) by applying cohesive forces on crack surfaces. Plasticity ahead of the crack tip was accounted for (Dugdale, 1960) by incorporating a strip of cohesive traction in front of the physical crack tip. Ungsuwarungsri and Knauss (1987) and Needleman (1990) were among the first to apply cohesive zone modeling to interfacial fracture. The approach was used to predict (Mohammed and Liechti, 2000) crack nucleation at bimaterial corners. The application of cohesive zone modeling requires the constitutive behavior of the interface to be defined as a separate constitutive entity from the bulk materials. The associated traction-separation relations typically consist of a linearly elastic response prior to damage initiation and a softening response associated with the degradation of the interface. Traction-separation relations for mode I and mode II were developed (Li et al., 2005, 2006) for the fracture of adhesively bonded polymer/matrix composite. Rate-dependent traction-separation relations were extracted (Zhu et al., 2009) for debonding of steel/polyurea/steel sandwich structures. A review paper (Stigh et al., 2010) summarized the experimental measurements required for and simulations with cohesive zone modeling in beam-like structures.

The toughness of the interface, which is the area underneath the traction-separation relation, has been used to predict the onset of fracture within the framework of linearly elastic fracture mechanics. The interfacial toughness depends on the stress state around the crack tip, which is governed by the mode-mix. The interfacial toughness usually rises as the contribution from mode II increases. Fracture tests on metal/epoxy systems obtained (Wang and Suo, 1990) higher toughness values at larger phase angles. The toughness of a glass/epoxy interface was measured (Liechti and Chai, 1992) over a wide range of mode-mix, and a strong toughening effect was observed with increasing shear components (positive and negative). Two main mechanisms contribute to the rise of the interface toughness with a stronger mode II effect. One explanation considered asperity locking between the interfaces (Evans and Hutchinson, 1989). Another mechanism was plastic dissipation (Swadener and Liechti, 1998b; Tvergaard and Hutchinson, 1993) where higher interface toughness can be attributed to more plastic work being dissipated ahead of the crack front.

In this paper, blister tests were used to determine the mixed-mode traction-separation relations for the interactions between thin films and substrates. The blister test was originally designed to measure the adhesion energy of thin films to their substrates (Dannenberg, 1958). The critical detachment pressure measured during the test (Hinkley, 1983) was used to calculate the adhesion energy of polymer films to silicon oxide. The ranges of applicability of membrane and plate analyses and their effect on yielding in blisters was examined (Liechti and Shirani, 1994). Jensen included the effect of residual stresses in the analysis of blister tests (Jensen, 1991; Jensen and Thouless, 1993) and later established the variation of mode-mix for blisters (Jensen, 1998). Cohesive zone modeling within the frame work of blister tests was considered in (Liechti et al., 2000; Shirani and Liechti, 1998). The mode-mix dependence of the adhesion energy of CVD grown graphene that had been transferred to copper and silicon was recently determined (Cao et al., 2015), where the effect of mode mix was attributed to asperity locking (Evans and Hutchinson, 1989). The current paper extends the investigation of mode-mix effects to the traction-separation relations governing the interactions between CVD graphene and copper. A range of mode-mix was achieved by varying the thickness of the blister film and a new set of measurements were introduced to track the normal crack opening displacements, blister radius and height using two separate microscopes with synchronized cameras.

2. Experiment

This section describes the specimen preparation and the apparatus that was used for obtaining the traction-separation relations for graphene/copper and photoresist/copper interfaces.

2.1. Specimen preparation

The mode-mix dependency of the traction-separation relations and adhesion energy for the interactions between transferred monolayer graphene and a polished copper substrate was first examined using a composite film of graphene coated with an epoxy photoresist SU-8 2025 (MicroChem Corporation). The purpose of the photoresist was to facilitate transfer of the graphene to the copper and reinforce it during pressurization. A range of mode-mix was achieved by changing the thickness of the photoresist. Blisters with the same photoresist but without graphene were used as a control.

A brief description on the specimen preparation is presented here and more details can be found in (Cao et al., 2014). The preparation of the photoresist started with depositing a thin copper film, roughly 100 nm thick, on a silicon wafer using a Denton thermal evaporation system. The operating pressure was approximately 10^{-6} Torr and the deposition rate was 1 Å/s. Photoresist layers of different thickness were spun on top of the copper film. Three different thicknesses, 10, 31, and 60 μm, were obtained by changing either the spin coating speed or the viscosity of the photoresist. The thickness of the film was measured by a profilometer (Dektak6M) with a vertical range and resolution of 260 μm and 10 nm, respectively. The sample was then soft-baked at 80 °C for 5 min. A razor blade was used to cut 5×5 cm grids on the photoresist film. The assembly was then submerged in an ammonium persulfate solution (1.0% wt.). The etchant flows through the trenches to etch away the copper underneath the photoresist. Finally, all the small squares of photoresist were sonicated in deionized water. In this way, optically flat photoresist films were obtained and each square was used to produce a circular blister on copper.

The films consisting of graphene coated with photoresist were prepared in the same fashion except that a monolayer of CVD graphene was first transferred to the same copper film on silicon substrate referred to above (Cao et al., 2014). The photoresist was applied, cured and diced as above to produce squares of graphene/photoresist. The etching process did not adversely affect the adhesion of graphene to the photoresist.

The next step was to transfer the film over a 3 mm diameter drilled hole in a copper substrate to produce layer that was in contact with the copper and suspended over the hole. After the transfer, the specimen was baked at 135 °C for 15 min with pressure being applied via a small weight. The weight prevented the heat flux from blowing off the membrane, and also improved the contact between the membrane and the substrate (Cao et al., 2014). The copper substrate was made of 101 oxygen-free, high-conductivity (OFHC) copper (Trident, Inc). The surface of the substrate was first polished with a range of sand papers, then by 3 μm, 1 μm, and 0.05 μm diamond compound pastes, until it was mirror-like. The root-mean-squared (RMS) roughness, as measured by atomic force microscopy (Cao et al., 2014), was 4.7 nm over a 10×10 μm area approximately 0.15 mm from the edge of the hole. The RMS roughness of three other areas nearby was 4.4, 4.1, and 3.9 nm. Deionized water and acetone were applied to clean the surface after polishing.

2.2. Apparatus

The film is pressurized (Fig. 1) with deionized water through a hole in the substrate using a syringe pump operating in volume

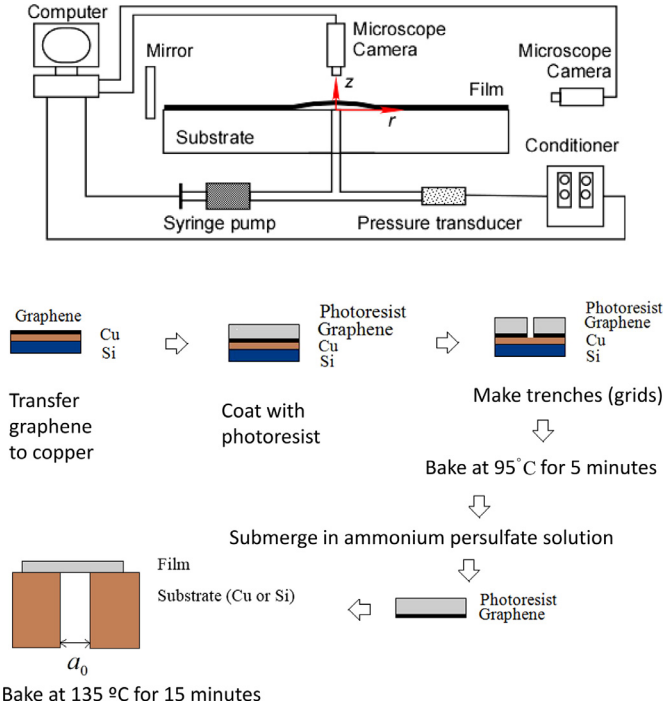

Fig. 1. Schematics of (a) the blister test apparatus for traction-separation relation experiments and (b) specimen fabrication.

control. Water is probably the most benign liquid to use in these experiments, with suitable viscosity and incompressibility characteristics for pressurization. Because there was no chemical bonding across the interface, the effect of water is probably minimal and thus not considered in the present study. There is also the possibility of a very small air pocket along the fronts of blisters.

Two microscopes with synchronized cameras measured the blister deflection and the NCOD near the crack fronts. Some common details of the apparatus and data processing can be found in our previous paper (Cao et al., 2014).

The major modification to the experiment was to simultaneously measure the blister profile and NCOD. The former (Fig. 2a) was measured by a horizontally mounted microscope (Wild M420 Macroscope) at 3x magnification with an Infinity 3-1 M digital camera. The specimen was placed on a tilting stage which had been carefully adjusted so that the total height of the blister could be observed. A reflective mirror was placed behind the sample to create a shadow and improve the brightness contrast between the outline of the blister and the background. The vertically mounted microscope made use of an Olympus 20x objective lens in order to measure the NCOD. The fringe pattern near the crack front (Fig. 2b) is due to the interference between the blister film and the substrate. The two cameras were synchronized so that the blister heights and NCOD were measured simultaneously. The initial blister diameter was chosen to be nominally 3 mm. This diameter provided the best resolution of blister profiles.

2.3. Measurements

The nominal resolution of the crack opening interferometry is λ/4 in transitioning from bright to dark fringes. The wavelength of light used here was 550 nm, yielding a nominal resolution of 137.5 nm. The NCOD (δ_n) between two adjacent fringes were determined from the light intensity I and the peak-to-peak intensity

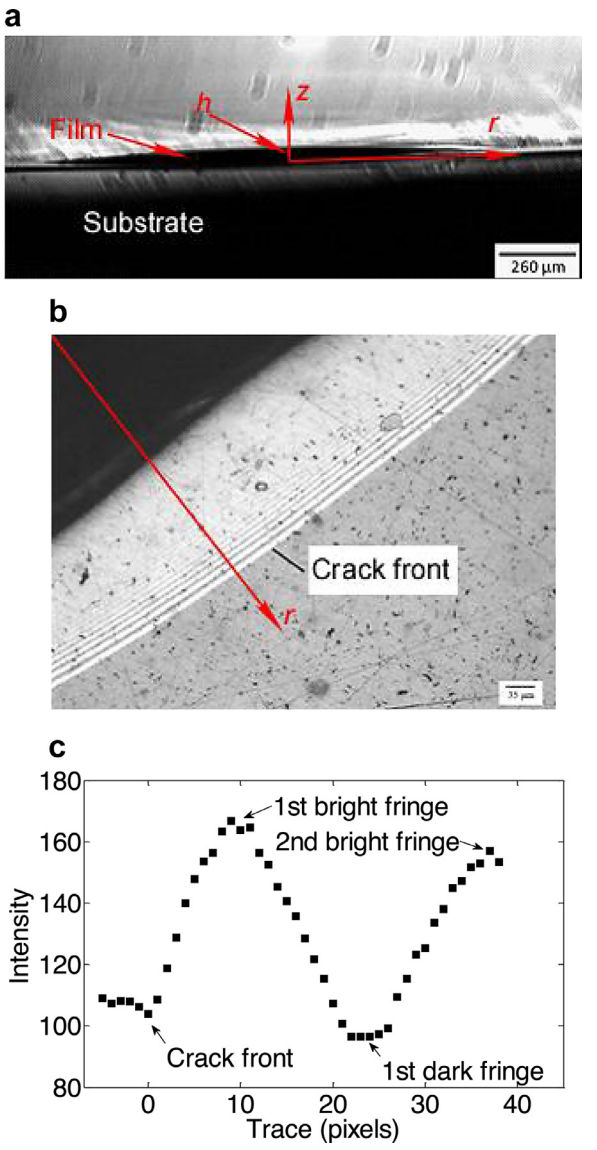

Fig. 2. (a) Blister profile of a photoresist film at 8.3 kPa pressure. (b) Fringe pattern near the crack tip at 8.3 kPa pressure. (c) Average of ten intensity profiles of NCOD from (b).

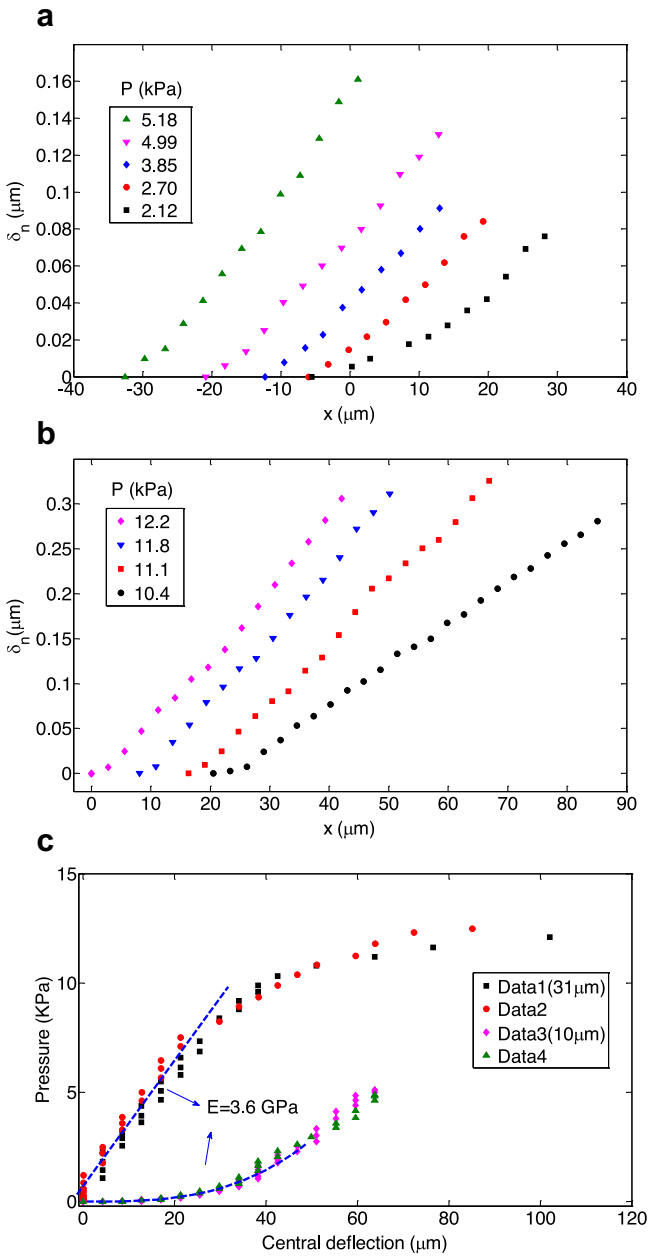

Fig. 3. Measurements of NCOD with film thickness of (a) 10 and (b) 31 μm, where the successive crack fronts at each pressure level are at zero separation; (c) Measured central deflection under various pressure.

I_{pp} through (Swadener and Liechti, 1998b)

$$\frac{I}{I_{pp}} = \frac{1}{2}\left[\pm 1 \mp \cos\left(\frac{4\pi|\delta_n|}{\lambda}\right)\right]. \tag{2.1}$$

This improves the resolution by more than an order of magnitude because more intensity data is being used than just the maxima and minima corresponding to individual fringes, bringing it down to approximately 10 nm. Fig. 2c shows the intensity profiles averaged over 10 pixel rows near the crack front. Approximately 10 data points were available between adjacent peaks and valleys. Fig. 3a and b are the NCOD obtained from light intensities using Eq. (2.1) with film thickness 10 and 31 μm, respectively.

Three values of film thickness, 10, 31, and 60 μm, were selected to determine the variation of traction-separation relations with mode-mix for both the graphene/copper and photoresist/copper interfaces. The measured central deflections and pressure levels are shown in Fig. 3c for film thicknesses of 10 and 31 μm, exhibiting membrane and plate behaviors, respectively. The discreteness of the height data indicates that it was determined by the number of pixels, increasing by 4.25 μm every time the blister height crossed a new pixel. The pressure-height response of the 31 μm thick films was initially linear, corresponding to the bulging of the blister without any delamination. The softening response at higher pressure values was due to the blister growth, which produces larger compliance. The increments of the blister radius were measured by the vertical camera, so the total radius of the blister was taken as $a = a_0 + \Delta a$, where a_0 was the initial blister radius prior to the application of pressure. The growth of the blister was quite symmetric. The blisters in this work were larger than before and beyond the field of view of the images, but a complete blister can be seen in (Cao et al., 2014) where smaller blisters were used. For the 10 μm thick film, the initial response was that of a membrane and subsequent softening was again attributed to delamination.

3. Theoretical analysis

This section describes the analyses that were conducted in order to obtain the adhesion energy and traction-separation relations associated with the interactions between graphene and copper as well as between photoresist and copper for comparison. Membrane and plate theories were used to obtain the energy release rates for thin and thicker films, respectively. A mixed-mode cohesive zone model was adopted, where the mode-mix was determined as a function of film thickness by finite element analysis in Section 4.

3.1. Blister deformation and adhesion energy

Membrane-like behavior was observed from the pressure (p) *vs.* central deflection (h) relationship for the film that was 10 μm thick (Fig. 3c). The membrane analysis (Yue et al., 2012) yields

$$p = \frac{Eth^3}{\phi a^4}, \tag{3.1}$$

where E is the Young's modulus of the film, ν is the Poisson's ratio, a is the blister radius, t is the film thickness and $\phi = \frac{75(1-\nu^2)}{8(23+18\nu-3\nu^2)}$. The energy release rate is related to the central deflection and radius of the blister through

$$G = \frac{5Eth^4}{8\phi a^4} \tag{3.2}$$

Plate-like behavior was observed for the films that were 31 and 60 μm thick (Fig. 3c). In this case, the relation between pressure and central deflection is (Yue et al., 2012)

$$p = \frac{64Bh}{a^4}, \tag{3.3}$$

where $B = \frac{Et^3}{12(1-\nu^2)}$ and the energy release rate is given by

$$G = \frac{32Bh^2}{a^4}. \tag{3.4}$$

In the blister test, the pressure was measured by a pressure transducer, and the blister radius was obtained from interferograms and the height from the profile measurement. Therefore, the Young's modulus of the photoresist was extracted once the thickness t had been measured by the profilometer. Fitting the thicker film data to Eq. (3.3) and using Eq. (3.1) for the thinner film yielded a Young's modulus of photoresist at 3.6 GPa, which was used in subsequent analysis and finite element simulations. Poisson's ratio was taken to be 0.35. The presence of a graphene monolayer for the composite film has a negligible effect on the modulus and Poisson's ratio. The energy release rate was obtained from Eq. (3.2) or Eq. (3.4) as a function of crack growth ($\Delta a = a - a_0$) giving the fracture resistance curve (Fig. 4).

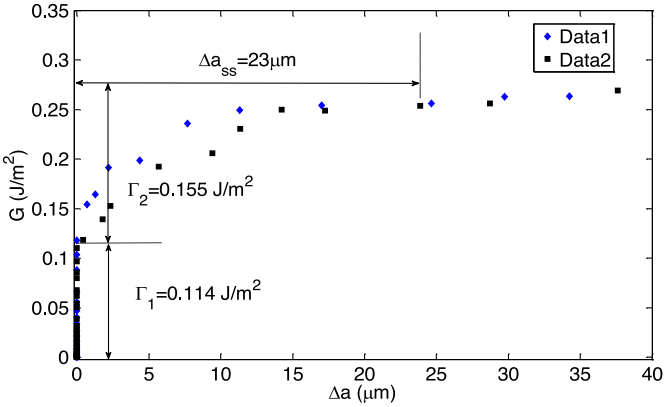

Fig. 4. Fracture resistance of photoresist/copper interface with a film thickness of 31 μm.

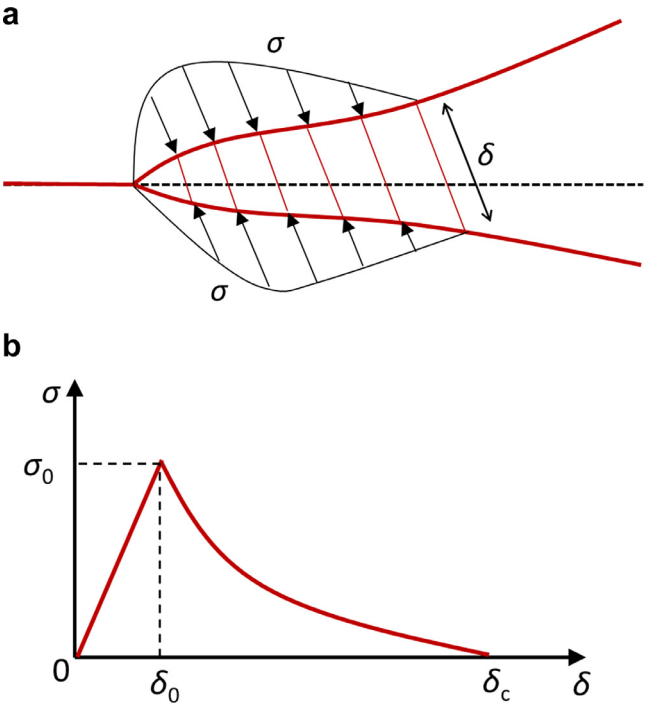

Fig. 5. (a) Schematic of a mixed-mode cohesive zone with vectorial traction and separation. (b) A traction-separation relation with exponential softening.

3.2. Cohesive zone models

In cohesive zone modeling, the normal and shear traction-separation relations for the interface are active in a region ahead of the physical crack front, which is the cohesive zone. The extent of the cohesive zone depends on the loading, crack geometry and the traction-separation relations and how they evolve, particularly in mixed-mode conditions. Consider a two-dimensional crack model with a cohesive zone (Fig. 5a). The traction in the cohesive zone has normal and shear components, labeled σ_n and σ_s, respectively. The relative displacement across the interface also has two components, δ_n and δ_s for the normal and shear crack opening displacement (NCOD and SCOD). The vectorial traction and separation are defined as

$$\sigma = \sqrt{\sigma_n^2 + \sigma_s^2} \text{ and } \delta = \sqrt{\delta_n^2 + \delta_s^2} \tag{3.5}$$

The rule associating σ with δ is called the traction-separation relation. Fig. 5b sketches a traction-separation relation with a linearly elastic relation followed by exponential softening. This is one of the simplest forms, although others have been used (Li et al., 2006). As the load is increased, the interface first opens elastically, following the elastic relation with an initial stiffness K_0 until the traction reaches the interfacial strength, at which point damage initiates and softening begins. The softening is described by a damage parameter D that increases monotonically from 0 (no damage) to 1 (complete damage). The damage remains constant if the crack is unloaded. Throughout the fracture process, the traction components are related to the separation as

$$\sigma_i = (1 - D)K_0\delta_i, \quad (i = n, s), \tag{3.6}$$

and the interface is regarded as having completely fractured when $D = 1$.

The mode-mix in the cohesive zone can be defined locally by the ratio between the two traction components:

$$\psi = \tan^{-1}\left(\frac{\sigma_s}{\sigma_n}\right). \tag{3.7}$$

This is equivalent to the definition based on the ratio between the two displacement components because the same stiffness K_0 is assumed for the two components. The use of the same stiffness ensures that the vectorial traction is in the same direction as the vectorial separation so that the interfacial fracture toughness can be calculated from the vectorial traction-separation relation as

$$\Gamma = \int_0^{\delta_c} \sigma \, d\delta, \tag{3.8}$$

where δ_c is the critical displacement as further discussed below. It can also be viewed as the range of the interactions between the surfaces. We note that the cohesive zone model adopted in this study is based on an irrecoverable damage model, where the evolution of the damage parameter depends on the loading path. This is different from cohesive models based on potential function, as noted by (Goutianos and Sørensen, 2012). To determine the mixed-mode traction-separation relations for a model based on irrecoverable damage (as the model used here), it is necessary to conduct the experiments and analysis under a proportional loading condition so that the mode-mix remains constant in each experiment. Once determined, the mixed mode traction-separation relations can be used for other loading paths.

With Eq. (3.6), the traction-separation relation depends primarily on the evolution of the damage parameter D, which is zero until damage initiates. Several criteria have been developed to define damage initiation and the maximum stress criterion was used for this study:

$$\max\left\{\left|\frac{\sigma_n}{\sigma_n^0}\right|, \left|\frac{\sigma_s}{\sigma_s^0}\right|\right\} = 1, \tag{3.9}$$

where σ_n^0 and σ_s^0 are the normal and shear strengths of the interface. The degradation of the material response will start once the damage initiation criterion is reached. In this study, it was found that damage initiation was dominated by the shear component so that $|\sigma_s| = \sigma_s^0$ and $\sigma_n = \sigma_s \cot\psi$ at the point of damage initiation for a particular mode mix. This leads to a mode-dependent interfacial strength for the vectorial traction-separation relation, $\sigma_0 = \sigma_s/|\sin\psi|$. Correspondingly, the vectorial separation at damage initiation is $\delta_0 = \sigma_0/K_0$.

After damage initiation, its evolution is described by an exponential softening function

$$D = 1 - \frac{\delta_0}{\delta_m}\left[1 - \frac{1 - \exp\left(-\alpha\dfrac{\delta_m - \delta_0}{\delta_c - \delta_0}\right)}{1 - \exp(-\alpha)}\right], \tag{3.10}$$

where δ_m is the maximal vectorial separation across the interface attained for any loading history ($\delta_m > \delta_0$), and α is a prescribed shape parameter for the exponential softening. The traction components can then be determined by substituting Eq. (3.10) into Eq. (3.6).

Damage evolution is complete when $\delta_m = \delta_c$ and $D = 1$, leaving a fully fractured interface at that location. The critical separation δ_c is related to the interfacial fracture toughness by Eq. (3.8). The interfacial fracture toughness Γ as defined in Eq. (3.8) can be decomposed into two parts, the toughness before damage initiation, $\Gamma_1 = \int_0^{\delta_0} \sigma \, d\delta$, and the ensuing toughness during damage evolution, $\Gamma_2 = \int_{\delta_0}^{\delta_c} \sigma \, d\delta$. For the exponential softening model, we obtain

$$\Gamma_1 = \frac{1}{2}\sigma_0\delta_0 \text{ and } \Gamma_2 = \sigma_0(\delta_c - \delta_0)\left(\frac{1}{\alpha} - \frac{1}{\exp(\alpha) - 1}\right) \tag{3.11}$$

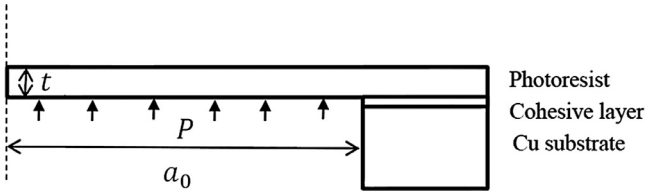

Fig. 6. Schematic of the axisymmetric finite element model of the blister test.

The decomposition of the interfacial toughness is illustrated in Fig. 4 where Γ_1 corresponds to the initiation energy at which the blister starts to delaminate, and Γ_2 corresponds to the additional energy required to reach the steady state toughness Γ_{ss} in the resistance curve. As will be shown later, this decomposition was used to extract the parameters in the traction-separation relations.

4. Finite element simulations

Axisymmetric finite element models were used to simulate the blisters (Fig. 6) using ABAQUS®. The thickness of the photoresist was denoted as t with its values being measured by a profilometer. The radius of the hole in the substrate was approximately 1.5 mm and experiments began with a slightly longer blister radius a_0 at zero pressure, with subsequent increases in pressure resulting in crack increment Δa. The outer radius of the substrate in the model was 2.5 mm, so the edge did not affect the delamination ($\Delta a \ll 1$ mm). The substrate was copper with a thickness of 80 μm. Graphene was not included in the model because it is extremely thin compared to the photoresist layer, but different traction-separation relations were assigned to graphene/copper and photoresist/copper interfaces. Axisymmetric, solid elements (CAX4R) were used in the entire model except the cohesive layer, where cohesive elements (COHAX4) with corresponding traction-separation relation were applied. The smallest elements were 5 nm by 5 nm, approximately 1/200th of the film thickness and small enough to resolve the cohesive zone. The maximum stress criterion (Eq. 3.9) was chosen for damage initiation. The damage evolution was the displacement type with exponential softening (Eq. 3.10).

The implementation of the cohesive zone model embodied in Eq. (3.5–10) in the finite element models was verified by comparing the interfacial stress state in the cohesive element closest to the crack front with the analytical model. This was illustrated in Fig. 7 for a 31 μm thick photoresist film interfacing with copper. The linear response prior to damage initiation had a stiffness $K_0 = 3.35 \times 10^{14}$ N/m^3, which was the same in the normal, shear, and vectorial traction-separation relations. The consistency between the finite element solutions and the analytical model was excellent in this regime. The softening process started once $|\sigma_s| = \sigma_s^0$reached 7.82 MPa, following the maximum stress criterion in Eq. (3.9). There was slight difference in the softening response of the normal traction-separation relation due to the assumption that the mode-mix was constant ($\sigma_s/\sigma_n = -1.7367$) during damage evolution, although this ratio did actually vary slightly. The other discrepancy was the critical separation, which ended earlier in the numerical results. This was due to the fact that the exponential traction-separation relation has a long and thin tail. The traction values drop to the computational noise level before the separation reaches the critical value. The early cut-off led to a small difference in the adhesion energy, *i.e.* the area underneath the traction-separation relation, for less than 1%.

5. Results and discussion

In this section, the variation of mode-mix with film thickness is first established, thereby setting the stage for exploring the mode-mix dependence of the adhesion energy and traction-separation

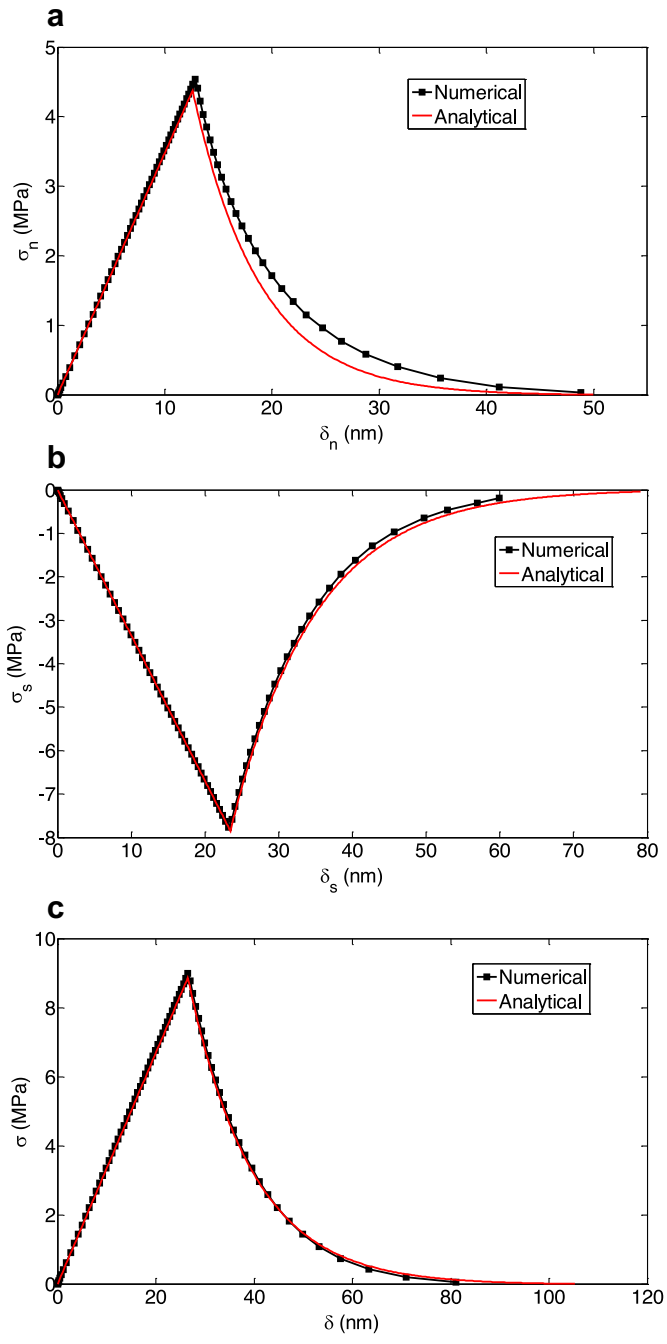

Fig. 7. Comparison of the analytical and numerical traction-separation relations for the photoresist/copper interface with a film thickness of 31 μm.

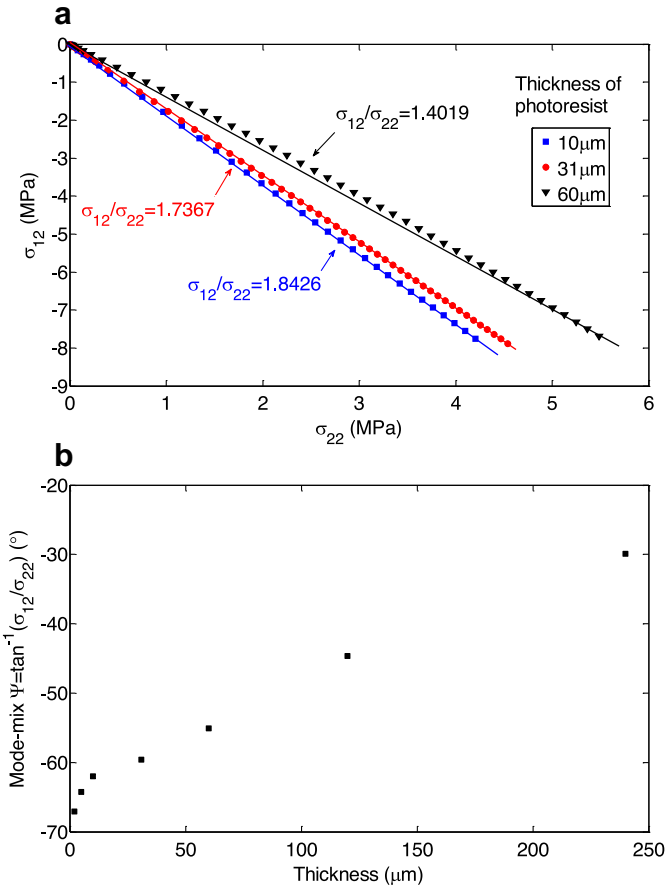

Fig. 8. (a) Normal and shear tractions, and (b) mode-mix of the blister tests with different layer thicknesses.

relations. Asperity locking, which had been identified as the cause of toughening with increasing shear component for the interfaces considered here (Cao et al., 2015), was used to develop traction-separation relations over a wider range of mode-mix. Another possibility for toughening under mixed-mode conditions is plastic dissipation in the photoresist (Swadener and Liechti, 1998a; Swadener, 1999). However, given the low pressure levels required to cause crack growth, the stresses in the photoresist were well below its yield strength.

5.1. Mode-mix

The variation of mode-mix defined in Eq. 3.7 was achieved by changing the film thickness. Fig. 8a shows the shear *versus* normal traction components at the crack tip by finite element simulations with three film thicknesses. As the pressure increases, the ratio between the two traction components remains nearly constant in each case, indicating a nearly constant mode-mix during each blister test. The traction ratios were −1.84, −1.74, and −1.40 for 10, 31, and 60 μm films, respectively, with corresponding phase angles of −62°, −60°, and −54° by definition in Eq. (3.7). The phase angles may depend on the specific cohesive zone model used in the finite element simulations. By using the damage-based cohesive zone model as described in Section 3.2, the obtained phase angles were found to be insensitive to the model parameters. The proportional loading of the blister test allows the mixed-mode traction-separation relation to be determined for each phase angle. Evidently, the shear traction becomes more dominant as the film becomes thinner. The relation between film thickness and mode-mix is presented over a broader range in Fig. 8b based on finite element simulations. The phase angle of mode-mix increased monotonically with slowing gradient as the film became thicker and the shear stress became less dominant. When the film was thicker than approximately 100 μm, the shear stress became smaller than the normal stress. When applying the maximum stress criterion in this domain and assuming the same strength in both directions ($\sigma_n^0 = \sigma_s^0$), it would be the normal stress, instead of the shear stress, that triggers damage initiation, although such a case was not tested in the present study. Fig. 8b suggests that approaching pure II is possible by using extremely thin films; however, the feasibility of doing so is unlikely due to difficulties in manufacturing and testing such thin films. Testing configurations other than the blister test will be required for pure mode I and II conditions.

Table 1
Parameters of the traction-separation relations associated with interactions between photoresist and copper and graphene and copper.

	Photoresist/copper			Graphene/copper		
	10 μm	31 μm	60 μm	10 μm	31 μm	60 μm
m	−1.8426	−1.7367	−1.4019	−1.8426	−1.7367	−1.4019
Γ_1 (J/m^2)	0.118	0.121	0.138	0.149	0.153	0.173
Γ_2 (J/m^2)	0.191	0.134	0.094	0.240	0.184	0.130
Δa_{ss} (μm)	27.52	23.36	18.60	26.18	21.55	15.81
σ_s^0 (MPa)	7.82	7.82	7.82	8.78	8.78	8.78
α	6	6	6	6	6	6
δ_c (nm)	158	117	91	177	141	105

5.2. Damage initiation and evolution

The parameters of the cohesive zone model were determined based on the blister tests. First, the damage initiation energy Γ_1 was taken directly from the resistance curve (see Fig. 5) as the energy at which the crack propagation initiated. By Eq. (3.11), the vectorial strength is $\sigma_0 = \sqrt{2\Gamma_1 K_0}$. The interfacial stiffness K_0 was chosen to be 3.35 × 10^{14}N/m for both shear and tension in all cases, which resulted in reasonable separation levels. Previous studies (Gowrishankar et al., 2012) have suggested that K_0 is a secondary parameter in the traction-separation relations. Let $m = \sigma_s/\sigma_n = \sigma_{12}/\sigma_{22}$, which was a constant for each specimen (Fig. 8). By the maximum stress criterion (Eq. 3.9), the interfacial shear strength σ_s^0 was determined as

$$\sigma_s^0 = |m|\sqrt{\frac{2\Gamma_1 K_0}{1+m^2}}. \tag{5.1}$$

Here, the strengths σ_n^0 and σ_s^0 were assumed to be the same, regardless of the mode-mix condition. As $m < -1$ in the thickness range considered here, damage initiated when the shear stress reached the strength ($|\sigma_s/\sigma_s^0| = 1$) and thus $\sigma_0 = \sigma_s^0\sqrt{1+m^{-2}}$.

The shear strength values obtained in this manner were 8.81, 8.95, 8.59 MPa for the graphene/copper interface, and 8.51, 7.57, 7.39 MPa for the photoresist/copper interface. The corresponding film thickness were 10, 31, and 60 μm. As the cohesive zone model assumes a constant shear strength for each interface, the average values of σ_s^0, 8.87 and 7.82 MPa for the two interfaces were used in the subsequent analysis. Accordingly, the values of Γ_1 and Γ_2 for each blister test were adjusted slightly as follows by using the average strength:

$$\begin{cases} \Gamma_1 = \dfrac{(\sigma_s^0)^2(1+m^2)}{2K_0 m^2} \\ \Gamma_2 = \Gamma_{ss} - \Gamma_1 \end{cases}. \tag{5.2}$$

The values of Γ_1 and Γ_2 are listed in Table 1 for the two interfaces, each with three film thicknesses.

In the experiments, the energy release rate was calculated from Eq. (3.2) or (3.4), depending on the thickness of the film. The location of crack tip was identified by the brightness contrast of the fringe pattern (Fig. 2b), and Δa_{ss} was the extent of blister growth before the energy release rate reached its steady state value in the resistance curve (Fig. 4). In the finite element simulations, the crack front was defined as the location where the damage initiated ($|\sigma_s/\sigma_s^0| = 1$), and Δa_{ss} corresponded to the steady-state cohesive zone size. The values of J-integral determined from the finite element analysis were in close agreement with those obtained from Eqs. (3.2) and (3.4) for the cases of membrane and plate behaviors, respectively.

Next, the parameters for exponential softening (Eq. 3.10) were determined for damage evolution. For each mode mix, the softening parameter α and the critical displacement δ_c were related to the toughness Γ_2 by Eq. (3.11). In addition, the value of Δa_{ss} associated with the resistance curve depends on the parameter α for given values of Γ_1 and Γ_2. To determine the two parameters (α and δ_c), a series of finite element analyses were conducted in which α was varied and the value of δ_c was determined from Eq. (3.11). The corresponding value of Δa_{ss} was obtained from the solution for the resistance curve. Fig. 9 shows the variation of Δa_{ss} as a function of α while maintaining the same values of Γ_1 and Γ_2 for a particular mode-mix. The appropriate values of α and δ_c were determined for each mode-mix by matching these values of Δa_{ss} with the measured ones (*e.g.* Fig. 4). It was found that α was essentially independent of mode-mix and a value of 6 was therefore assigned to both interfaces. All the parameters for exponential softening determined in this way are listed in Table 1.

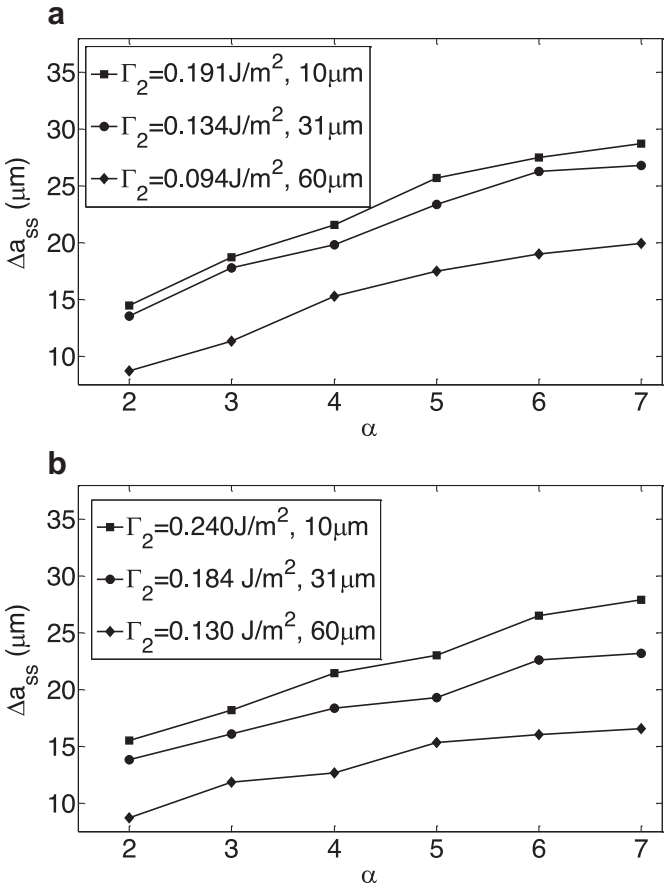

Fig. 9. Variation of Δa_{ss} as a function of the softening parameter α for (a) photoresist/copper and (b) graphene/copper interfaces.

The next step was to conduct a series of finite element analyses using the deduced parameters for the two interfaces (Table 1) and compare the numerical results with the measurements as a validation of the cohesive zone model. First, the resistance curves are compared for photoresist/copper (Fig. 10) and graphene/copper (Fig. 11) interfaces, respectively. The numerical results agreed with the data reasonably well. The small discrepancy in the damage initiation was due to the fact that Γ_1 in the traction-separation relation was adjusted in Eq. (5.2) in order to maintain the same shear strength for all mode-mixes. The transition from damage initiation to steady state crack growth was captured remarkably well in all cases, which indicates that the procedure for selecting the softening parameter α worked well. As indicated earlier in describing the experiments, it was possible to obtain crack growth beyond steady state because the loading device was operating nominally in volume control. However, in the finite element analysis, the

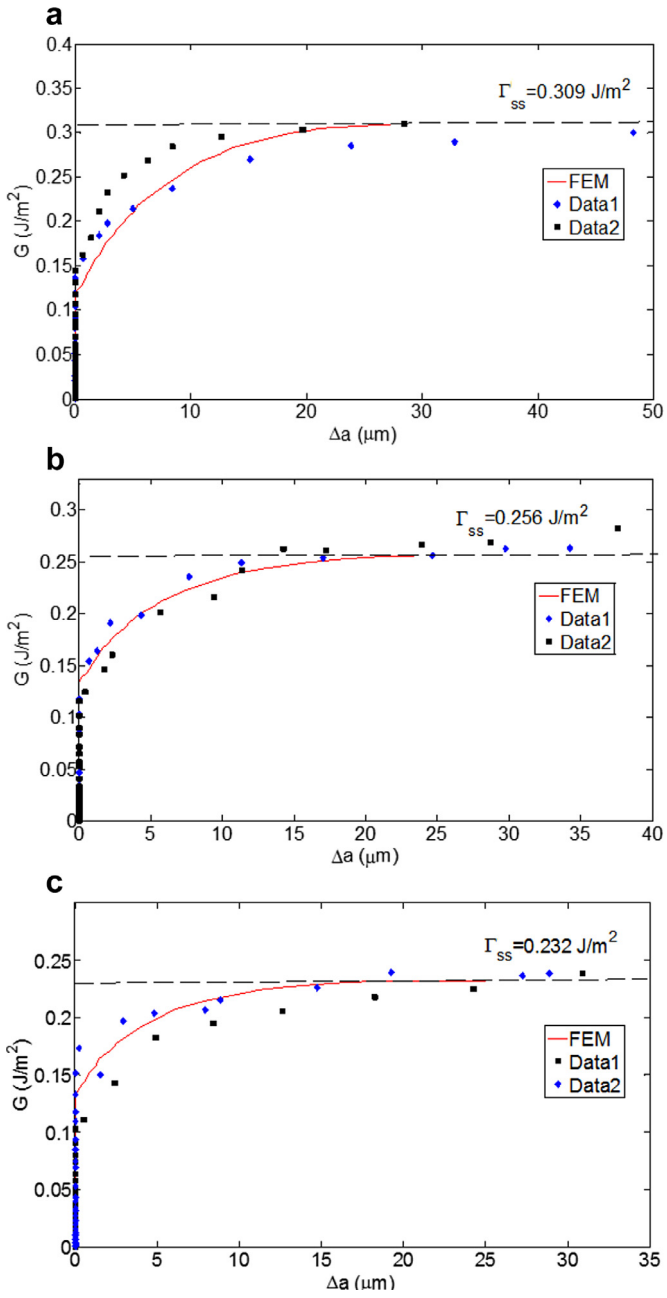

Fig. 10. Comparison of resistance curves for the photoresist/copper interface with different layer thickness, (a) 10, (b) 31, and (c) 60 μm.

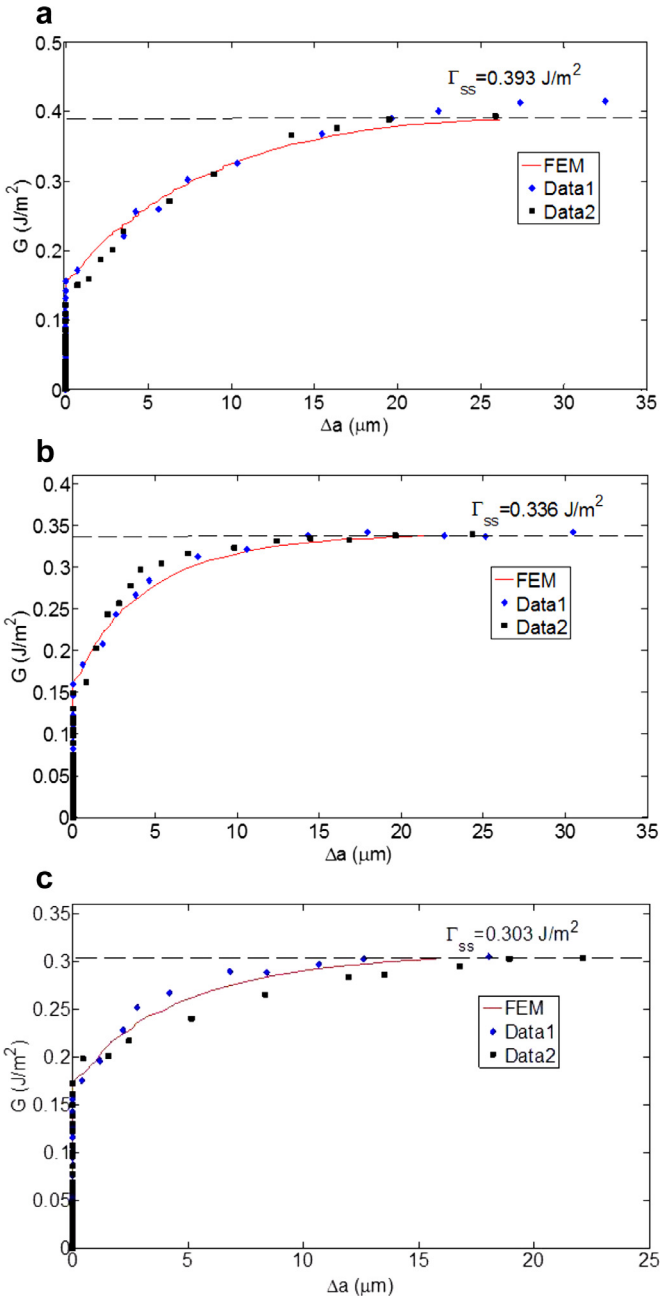

Fig. 11. Comparison of resistance curves for the graphene/copper interface with different layer thickness, (a) 10, (b) 31, and (c) 60 μm.

solution progressed under pressure control, which is inherently unstable for blisters. Nonetheless it was possible to obtain stable growth slightly beyond Δa_{ss} as can be seen in Figs. 10 and 11.

The solutions for the variation of the central deflections of the graphene/photoresist blisters with pressure were compared with measurements in Fig. 12. The bare photoresist blisters behaved similarly, hence not shown. For those specimens whose film thickness was 10 μm, the blisters exhibited membrane behavior (Fig. 12a) with the pressure and the central deflection following $p \sim h^3$ (Eq. 3.1). The plate response in pressure *vs.* central deflection was evident for blisters that were 31 and 60 μm thick (Fig. 12b and c). The linear response was associated with bulging of the blister, and the subsequent softening response was due to delamination, which actually initiated near the end of the linear response in a gradual departure from linearity.

Further comparisons are made between the experimental and numerical results for the NCOD in Figs. 13 and 14 as a function of pressure. In all cases, the location $x = 0$ was the location of the initial crack front at zero applied pressure, with $x < 0$ corresponding to radial locations ahead of the crack front. As the pressure was increased, a cohesive zone developed and extended ahead of the physical crack front with the damage parameter, $1 > D > 0$, until D reached one at the crack front, and subsequently steady state crack growth ensued. It is possible to track the locations of the elastically deforming ($D = 0$), partially damaged ($0 < D < 1$) and fully damaged regions in the numerical solutions. In the numerical analysis, the crack front was defined as the damage initiation point where the NCOD was $\sigma_s^0/(mK_0)$, as noted by the lower dashed line in each figure. The NCOD in the elastically deforming portion of the cohesive zone lie below this line and essentially ex-

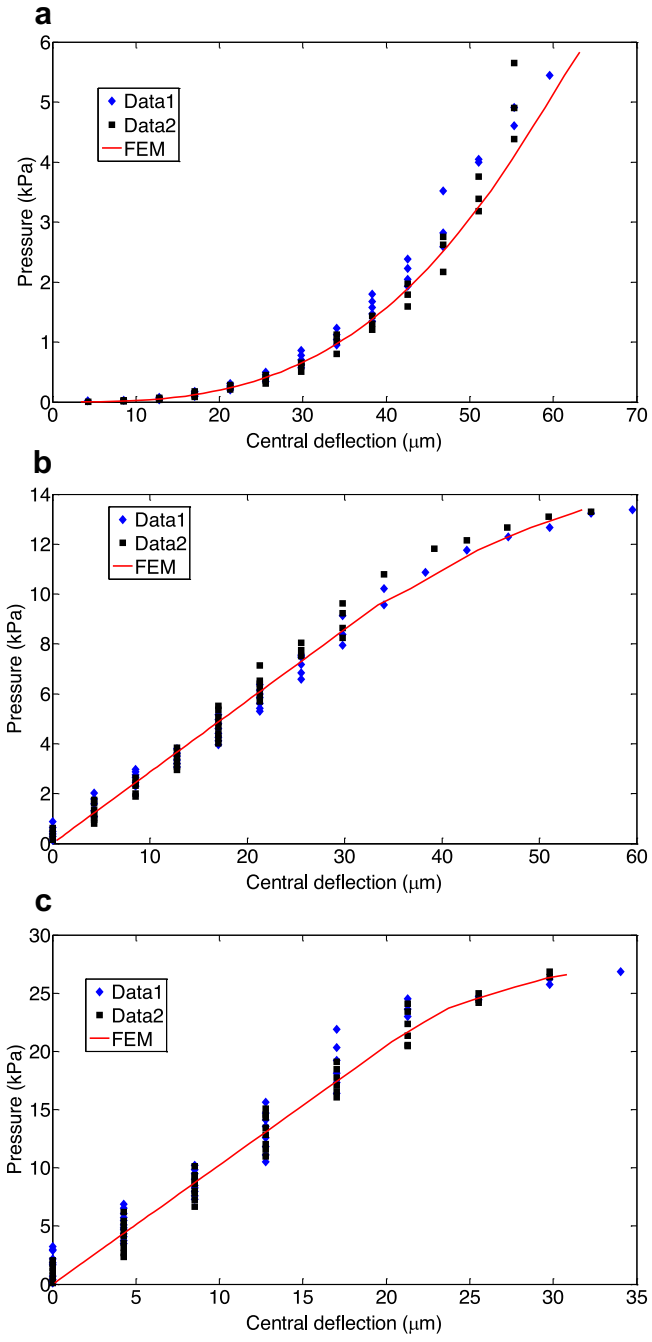

Fig. 12. Variation of pressure with central deflection for graphene/photoresist films of different thicknesses, (a) 10, (b) 31, and (c) 60 μm.

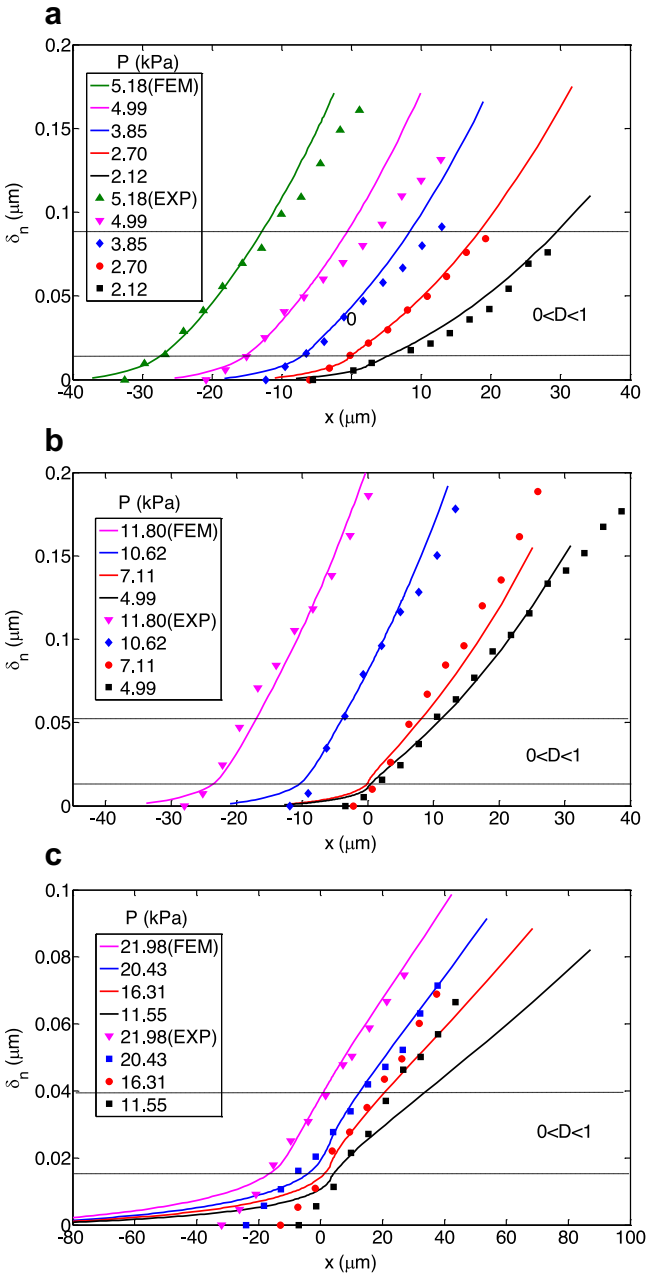

Fig. 13. Comparison of numerical solutions and measured NCOD for photoresist/copper interfaces with film thickness of (a) 10, (b) 31, and (c) 60 μm.

tend far ahead of the crack front, but are not always measurable due to the resolution of the interferometry. The upper dashed line was the value of the NCOD at which damage evolution just completed (*i.e.* $D = 1$ and $\delta_n = \delta_c/\sqrt{1+m^2}$), which was also the end of the cohesive zone. The situation is less obvious for the measured NCOD, which carry no clear indication of the transitions and even the location of the crack front carries some uncertainty due to spatial resolution in the measurements (±1 pixel, 2.25 μm). The measured locations of zero NCOD noted in each graph were positioned within this uncertainty so as to obtain the best fit between the numerical solutions for NCOD and the measurements further behind the crack front. As the films became thicker, the length of the elastic region increased and there was a more notable transition from the elastic region to the damaged region, which was captured by both the numerical solutions and the measurements. This response is plausible, because a thicker film is more difficult to bend.

The vectorial traction-separation relations obtained for the three phase angles (−54°, −60° and −62°) corresponding to the three film thicknesses in the experiments are shown in Fig. 15. Also shown are the predicted traction-separation relations for phase angles beyond the range accessible to the blister tests in this study. The extension was obtained based on the following assumptions: (1) The elastic stiffness and the maximum strength was the same for the normal and shear components. Thus damage initiation and Γ_1 for extended phase angles were obtained in the same manner as before with $\Gamma_1 = \Gamma_1^0(1+m^2)$ if $|m| \le 1$ and $\Gamma_1 = \Gamma_1^0(1+m^{-2})$ if $|m| \ge 1$, where $\Gamma_1^0 = (\sigma_s^0)^2/(2K_0)$. (2) The exponential softening parameter $\alpha = 6$, and the critical separation δ_c depends on the mode-mix through Eq. (3.11), where $\Gamma_2 = \Gamma_{ss} - \Gamma_1$

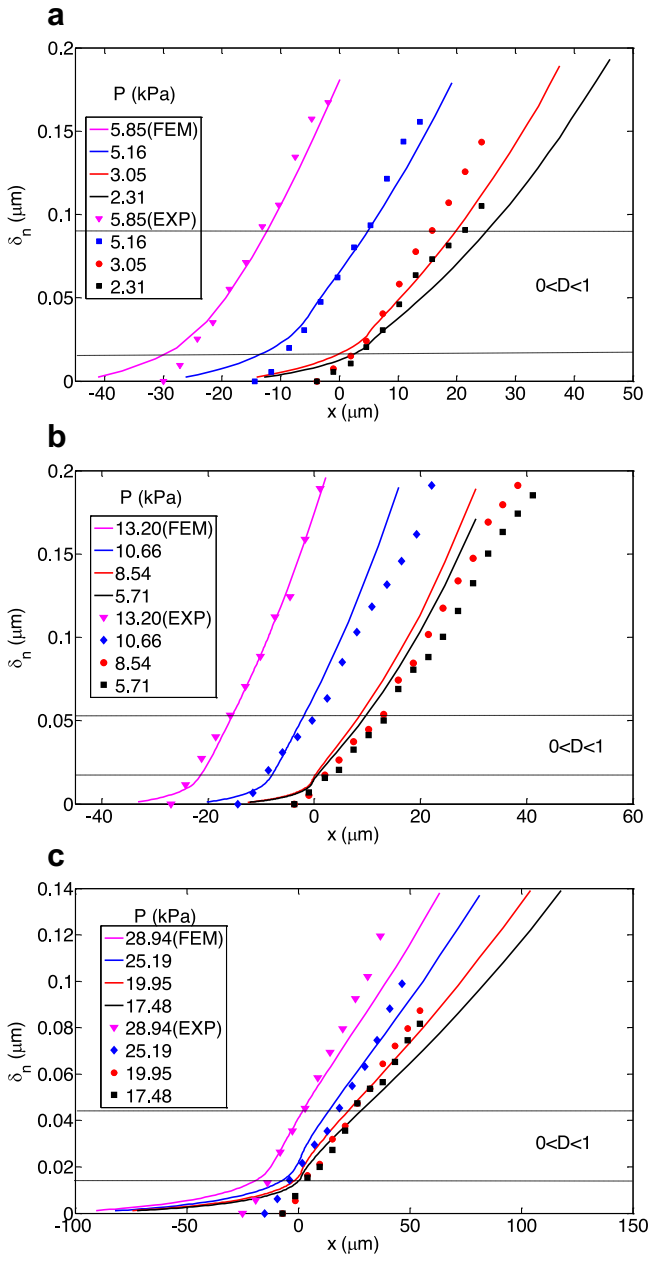

Fig. 14. Comparison of numerical solutions and measured NCOD for graphene/copper interfaces with film thickness of (a) 10, (b) 31, and (c) 60 μm.

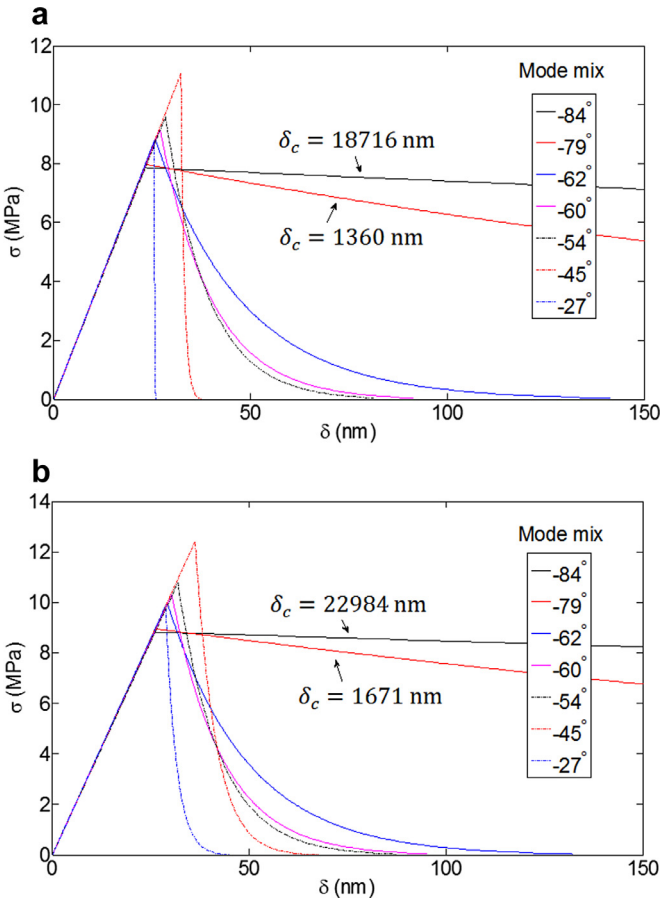

Fig. 15. The vectorial traction-separation relations of (a) photoresist/copper and (b) graphene/copper interfaces under different mixed-mode conditions.

and Γ_{ss} is the steady-state adhesion energy obtained from the asperity locking model. It was shown in a previous study that the asperity locking model (Evans and Hutchinson, 1989) had provided a good explanation of the toughening effect over a wider range of phase angles (Cao et al., 2015). The effect of asperity locking on the adhesion energy was given by Evans and Hutchinson (1989)

$$\frac{\Delta\Gamma_{SS}}{\Gamma_{SS}} = \frac{\tan^2\psi\left\{1-\kappa^2(\alpha)\right\}}{1+\tan^2\psi}, \tag{5.3}$$

where $\Delta\Gamma_{ss} = \Gamma_{ss} - \Gamma^0_{ss}$, $\alpha = \alpha_0(1+\tan^2\psi)(1-\Delta\Gamma_{SS}/\Gamma_{SS})$ and $\kappa(\alpha)$ is a function given implicitly in (Budiansky et al., 1988).[1] For undulating crack surfaces, $\alpha_0 = 0.1EH/\Gamma^0_{ss}(1-\nu^2)$, where E was taken to be the tensile modulus of the photoresist, H the RMS roughness of the crack faces or interface, and Γ^0_{ss} is the mode-I toughness. The average values of Γ^0_{ss} extracted from Eq. (5.3) and the toughness data from the experiments conducted at three mode-mixes for the graphene/copper and photoresist/copper interfaces were 0.0916 and 0.0667 J/m^2, respectively. The RMS roughness of the polished copper substrates was 4.4 nm and the tensile modulus of the photoresist of 3.6 GPa, thus yielding values of α_0 at 14.9 and 20.4. As noted in (Evans and Hutchinson, 1989), when $\alpha_0 > 1$, Eq. (5.3) simplifies to

$$\frac{\Delta\Gamma_{SS}}{\Gamma_{SS}} = \frac{\tan^2\psi}{1+\tan^2\psi} \tag{5.4}$$

The toughness envelope for the two interfaces by Eq. (5.4) is shown in Fig. 16, where the fit to the admittedly limited data is quite good.

As a result, the extended model predicted that the interfacial toughness approaches infinity at $\psi = \pm 90^\circ$ (mode II). On the other hand, the maximum vectorial strength occurred at $\psi = \pm 45^\circ$ at 11.06 and 12.42 MPa (Table 2) for the photoresist/copper and graphene/copper interfaces, respectively. As shown in Fig. 15, the maximum strength was followed by a very sharp softening behavior to interaction ranges of 33 and 64 nm, respectively. The corresponding adhesion energies were 0.132 and 0.182 J/m^2. Thus the interaction between graphene and copper had a higher adhesion energy, strength and range for this and all mode-mixes. Some contact angle measurements (Rafiee et al., 2012) and simulations (Shih et al., 2013) have suggested that graphene is either transparent to or partially masks the interactions between materials adjacent to graphene. Based on the current study, we can say that graphene

[1] Note that this corresponds to Eq. (40) in (Evans and Hutchinson, 1989), where there was a typographical error in that $\kappa(\alpha)$ was not squared as it should be. This error was missed in applying Eq. (40) in Cao et.al. (2015).

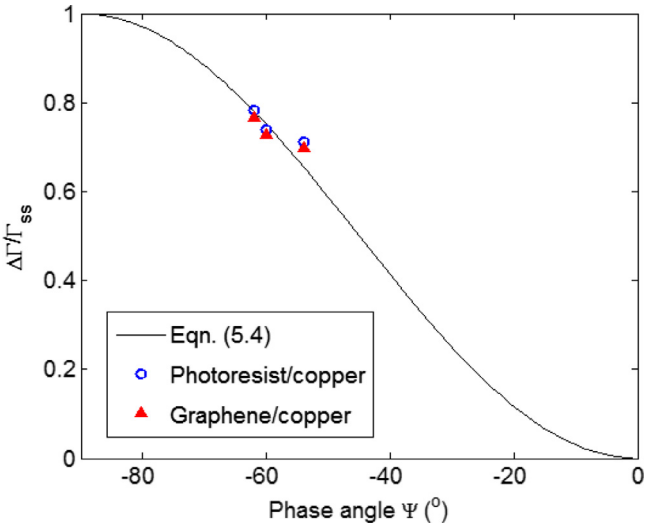

Fig. 16. The toughness envelope for photoresist/copper and graphene/copper interfaces.

Table 2
Traction-separation relation parameters at $\psi = -45^{\circ}$.

Property	Graphene/copper	Photoresist/copper
Γ_{ss} (J/m^2)	0.182	0.132
σ_0 (MPa)	12.42	11.06
δ_c (nm)	63.9	33.4

is not transparent to the interactions, but may partially or completely mask the interactions. Graphene has also been observed to partially screen the force field between a diamond probe tip and silicon oxide in displacement-controlled nano indentation experiments (Suk et al., 2015). Although contact between solid bodies is closer to fracture than contact angle experiments, in the present study graphene did screen the interactions between photoresist and copper. In fact, because the interactions were stronger in all aspects (adhesion energy, strength and range), it can be argued that graphene acted as an opaque layer in this instance and all that we are seeing is the interaction between graphene and copper.

The interaction ranges δ_c for the specimens that were considered ranged from 90 to 180 nm and are clearly well beyond the 10 nm range normally associated with van der Waals interactions. The normal components of the interaction ranges were between 40 and 100 nm (see Figs. 13 and 14). The RMS roughness of the copper prior to deposition of the graphene was 4.4 nm, so it is not clear that this is reflected in the interaction range. It is also possible that very small amounts of moisture were still trapped at the graphene/copper interface, in spite of the baking process following transfer. This would bring capillary effects into play with longer interaction ranges, particularly in separation. Further studies are needed to understand the underlying mechanisms of such long-range interactions.

According to the extension scheme, the interaction ranges became significantly longer with increasing phase angle (toward mode II) and was 18.7 μm at $\psi = -84^{o}$. The interaction range in shear would have to accommodate shear deformation of asperities, so the increase is certainly expected. In trying to extend the model to mode I dominant conditions $|\psi| < 45^{o}$, the most that could be accommodated was $|\psi| = 27^{o}$. For phase angles closer to zero, the fracture toughness obtained from Eq. (5.4) was smaller than the initiation energy Γ_1 and other test configurations will be required to explore the interactions closer to mode I.

6. Conclusions

A modified blister test was developed to obtain the traction-separation relations for graphene/copper and photoresist/copper interfaces. One microscope and camera measured the blister radius and NCOD by viewing from the top, while a second one, equipped with a synchronized camera, measured the blister height from the side. The data from such measurements over a range of mixed-mode conditions were converted to fracture resistance curves of the interfaces using linear plate or membrane analysis. A systematic approach to extract traction-separation relations from resistance curves using cohesive zone modeling was established. The parameters associated with traction-separation relations with exponential softening were determined from Γ_1 the damage initiation energy, Γ_2 the additional energy dissipated before reaching steady state, and Δa_{ss} the transition length from initiation to steady state in the resistance curves. Three mixed-mode conditions were investigated for both photoresist/copper and graphene/copper interfaces by using three different film thicknesses. These results allowed for mixed-mode effects to be accounted for in the traction-separation relations by requiring that initiation was governed by the maximum normal or shear strength, which were both independent of mode-mix. The softening parameter, which governed damage evolution, was also independent of mode-mix. On the other hand, both the vectorial strength and interaction range depend on mode mix. When these conditions were incorporated in numerical models of the test configurations, solutions for pressure *vs.* crack and blister height and NCOD were all in good agreement with measurements. The model was extended to other mode-mixes by making use of the asperity locking model which had provided a mechanism for the observed toughening effect. The interactions between graphene and copper were stronger in all respects than those associated with photoresist and copper. Because the monolayer graphene was sandwiched between photoresist and copper, this result suggests that graphene was not completely transparent to interactions between photoresist and copper. Moreover, the range of the measured and predicted interactions was remarkably long, certainly beyond van der Waals interactions, but possibly indicating capillary effects, modulated by roughness, as suggested by the efficacy of the asperity locking model.

Acknowledgments

The authors gratefully acknowledge partial financial support of this work by the National Science Foundation through Grant no. CMMI-1130261. This work is also based upon work supported in part by the National Science Foundation under Cooperative Agreement no. EEC-1160494. Any opinions, findings and conclusions or recommendations expressed in this material are those of the author(s) and do not necessarily reflect the views of the National Science Foundation.

References

Allen, M.J., Tung, V.C., Kaner, R.B., 2009. Honeycomb carbon: a review of graphene. Chem. Rev. 110, 132–145.
Barenblatt, G.I., 1959. Equilibrium cracks formed on a brittle fracture. Dokl Akad Nauk Sssr+ 127, 47–50.
Budiansky, B., Amazigo, J.C., Evans, A.G., 1988. Small-scale crack bridging and the fracture toughness of particulate-reinforced ceramics. J. Mech. Phys. Solids 36, 167–187.
Cao, Z., Tao, L., Akinwande, D., Huang, R., Liechti, K.M., 2015. Mixed-mode interactions between graphene and substrates by blister tests. J. Appl. Mech. 82 081008–081008.
Cao, Z., Wang, P., Gao, W., Tao, L., Suk, J.W., Ruoff, R.S., Akinwande, D., Huang, R., Liechti, K.M., 2014. A blister test for interfacial adhesion of large-scale transferred graphene. Carbon 69, 390–400.

Cicero, G., Grossman, J.C., Schwegler, E., Gygi, F., Galli, G., 2008. Water confined in nanotubes and between graphene sheets: a first principle study. J. Am. Chem. Soc. 130, 1871–1878.
Dannenberg, H., 1958. Measurement of adhesion by a blister method. J Polym Sci 33, 509–510.
Dugdale, D.S., 1960. Yielding of steel sheets containing slits. J. Mech. Phys. Solids 8, 100–104.
Dundurs, J., Bogy, D.B., 1969. Edge-bonded dissimilar orthogonal elastic wedges under normal and shear loading. J. Appl. Mech. 36, 650–652.
Erdogan, F., 1965. Stress distribution in bonded dissimilar materials with cracks. J. Appl. Mech. 32, 403–410.
Evans, A.G., Hutchinson, J.W., 1989. Effects of non-planarity on the mixed mode fracture resistance of bimaterial interfaces. Acta Metall 37, 909–916.
Gao, W., Huang, R., 2011. Effect of surface roughness on adhesion of graphene membranes. J. Phys. D: Appl. Phys. 44, 452001.
Gao, W., Liechti, K.M., Huang, R., 2015. Wet adhesion of graphene. Extrem. Mech. Lett. 3, 130–140.
Gao, W., Xiao, P., Henkelman, G., Liechti, K.M., Huang, R., 2014. Interfacial adhesion between graphene and silicon dioxide by density functional theory with van der Waals corrections. J. Phys. D: Appl. Phys. 47, 255301.
Geim, A.K., Novoselov, K.S., 2007. The rise of graphene. Nat. Mater. 6, 183–191.
Goutianos, S., Sørensen, B.F., 2012. Path dependence of truss-like mixed mode cohesive laws. Eng. Fract. Mech. 91, 117–132.
Gowrishankar, S., Mei, H.X., Liechti, K.M., Huang, R., 2012. A comparison of direct and iterative methods for determining traction-separation relations. Int. J. Fract. 177, 109–128.
Hinkley, J.A., 1983. A blister test for adhesion of polymer films to $Si0_2$. J. Adhes. 16, 115–125.
Hutchinson, J.W., Suo, Z., 1992. Mixed-mode cracking in layered materials. Adv. Appl. Mech. 29, 63–191.
Jensen, H.M., 1991. On the blister test for interface toughness measurement. Eng. Fract. Mech. 40, 475–486.
Jensen, H.M., 1998. Analysis of mode mixity in blister tests. Int. J. Fract. 94, 79–88.
Jensen, H.M., Thouless, M.D., 1993. Effects of residual stress in the blister test. Int. J. Solids Struct. 30, 779–795.
Koenig, S.P., Boddeti, N.G., Dunn, M.L., Bunch, J.S., 2011. Ultrastrong adhesion of graphene membranes. Nat. Nanotechnol. 6, 543–546.
Leenaerts, O., Partoens, B., Peeters, F.M., 2009. Water on graphene: hydrophobicity and dipole moment using density functional theory. Phys. Rev. B 79, 235440.
Li, G.X., Yilmaz, C., An, X.H., Somu, S., Kar, S., Jung, Y.J., Busnaina, A., Wan, K.T., 2013. Adhesion of graphene sheet on nano-patterned substrates with nano-pillar array. J. Appl. Phys. 113.
Li, S., Thouless, M.D., Waas, A.M., Schroeder, J.A., Zavattieri, P.D., 2005. Use of mode-I cohesive-zone models to describe the fracture of an adhesively-bonded polymer-matrix composite. Compos. Sci. Technol. 65, 281–293.
Li, S., Thouless, M.D., Waas, A.M., Schroeder, J.A., Zavattieri, P.D., 2006. Mixed-mode cohesive-zone models for fracture of an adhesively bonded polymer-matrix composite. Eng. Fract. Mech. 73, 64–78.
Liechti, K.M., Chai, Y.S., 1992. Asymmetric shielding in interfacial fracture under in-plane shear. J. Appl. Mech.-Trans. ASME 59, 295–304.
Liechti, K.M., Shirani, A., 1994. Large scale yielding in blister specimens. Int. J. Fract. 67, 21–36.
Liechti, K.M., Shirani, A., Dillingham, R.G., Boerio, F.J., Weaver, S.M., 2000. Cohesive zone models of polyimide/aluminum interphases. J. Adhes. 73, 259–297.
Lui, C.H., Liu, L., Mak, K.F., Flynn, G.W., Heinz, T.F., 2009. Ultraflat graphene. Nature 462, 339–341.
Mohammed, I., Liechti, K.M., 2000. Cohesive zone modeling of crack nucleation at bimaterial corners. J. Mech. Phys. Solids 48, 735–764.
Na, S.R., Suk, J.W., Ruoff, R.S., Huang, R., Liechti, K.M., 2014. Ultra long-range interactions between large area graphene and silicon. Acs Nano 8, 11234–11242.
Needleman, A., 1990. An analysis of tensile decohesion along an interface. J. Mech. Phys. Solids 38, 289–324.
Novoselov, K.S., Fal, V., Colombo, L., Gellert, P., Schwab, M., Kim, K., 2012. A roadmap for graphene. Nature 490, 192–200.
Novoselov, K.S., Geim, A.K., Morozov, S.V., Jiang, D., Zhang, Y., Dubonos, S.V., Grigorieva, I.V., Firsov, A.A., 2004. Electric field effect in atomically thin carbon films. Science 306, 666–669.
Rafiee, J., Mi, X., Gullapalli, H., Thomas, A.V., Yavari, F., Shi, Y., Ajayan, P.M., Koratkar, N.A., 2012. Wetting transparency of graphene. Nat. Mater. 11, 217–222.
Randviir, E.P., Brownson, D.A., Banks, C.E., 2014. A decade of graphene research: production, applications and outlook. Mater. Today 17, 426–432.
Rice, J.R., 1988. Elastic fracture mechanics concepts for interfacial cracks. J. Appl. Mech. 55, 98–103.
Rudenko, A.N., Keil, F.J., Katsnelson, M.I., Lichtenstein, A.I., 2011. Graphene adhesion on mica: role of surface morphology. Phys. Rev. B 83.
Shih, C.-J., Strano, M.S., Blankschtein, D., 2013. Wetting translucency of graphene. Nat. Mater. 12, 866–869.
Shirani, A., Liechti, K.M., 1998. A calibrated fracture process zone model for thin film blistering. Int. J. Fract. 93, 281–314.
Stigh, U., Alfredsson, K.S., Andersson, T., Biel, A., Carlberger, T., Salomonsson, K., 2010. Some aspects of cohesive models and modelling with special application to strength of adhesive layers. Int. J. Fract. 165, 149–162.
Suk, J.W., Na, S.R., Stromberg, R.J., Stauffer, D., Lee, J., Ruoff, R.S., Liechti, K.M., 2015. Probing the adhesion interactions of graphene on silicon oxide by nanoindentation. ACS Nano, Carbon, in review.
Suresh, S., Shih, C.F., Morrone, A., O'Dowd, N.P., 1990. Mixed-mode fracture-toughness of ceramic materials. J. Am. Ceram. Soc. 73, 1257–1267.
Swadener, J., Liechti, K., 1998a. Asymmetric shielding mechanisms in the mixed-mode fracture of a glass/epoxy interface. J. Appl. Mech. 65, 25–29.
Swadener, J.G., Liechti, K.M., 1998b. Asymmetric shielding mechanisms in the mixed-mode fracture of a glass/epoxy interface. J. Appl. Mech. 65, 25–29.
Swadener, J.G., Liechti, K.M., de Lozanne, A.L., 1999. The intrinsic toughness and adhesion mechanism of a glass/epoxy interface. J. Mech. Phys. Solids 47, 223–258.
Tvergaard, V., Hutchinson, J.W., 1993. The influence of plasticity on mixed-mode interface toughness. J. Mech. Phys. Solids 41, 1119–1135.
Ungsuwarungsri, T., Knauss, W.G., 1987. The role of damage-softened material behavior in the fracture of composites and adhesives. Int. J. Fract. 35, 221–241.
Wang, J.S., Suo, Z., 1990. Experimental-determination of interfacial toughness curves using Brazil-nut-sandwiches. Acta Metall. Mater. 38, 1279–1290.
Wehling, T.O., Lichtenstein, A.I., Katsnelson, M.I., 2008. First-principles studies of water adsorption on graphene: the role of the substrate. Appl. Phys. Lett. 93, 202110.
Williams, M.L., 1959. The stress around a fault or crack in dissimilar media. Bull. Seismol. Soc. Am. 49, 199–204.
Yue, K., Gao, W., Huang, R., Liechti, K.M., 2012. Analytical methods for the mechanics of graphene bubbles. J. Appl. Phys. 112, 083512.
Zhu, Y., Liechti, K.M., Ravi-Chandar, K., 2009. Direct extraction of rate-dependent traction-separation laws for polyurea/steel interfaces. Int. J. Solids Struct. 46, 31–51.
Zong, Z., Chen, C.L., Dokmeci, M.R., Wan, K.T., 2010. Direct measurement of graphene adhesion on silicon surface by intercalation of nanoparticles. J. Appl. Phys. 107, 026104.